

Article

Novel Indium Vanadium Oxide Nanosheet-Supported Nickel Iron Oxide Nanoplate Heterostructure for Synergistically Enhanced Photocatalytic Degradation of Tetracycline

N. Sreeram ¹, V. Aruna ^{1,2,*}, Ravindranadh Koutavarapu ^{3,*} , Dong-Yeon Lee ^{3,*} and Jaesool Shim ^{4,*}

¹ Department of Physics, Acharya Nagarjuna University, Nagarjuna Nagar, Guntur 522 510, Andhra Pradesh, India

² Department of Physics, Bapatla Engineering College, Bapatla 522 102, Andhra Pradesh, India

³ Department of Robotics Engineering, College of Mechanical and IT Engineering, Yeungnam University, Gyeongsan 38541, Republic of Korea

⁴ School of Mechanical Engineering, Yeungnam University, Gyeongsan 38541, Republic of Korea

* Correspondence: verreddigariaruna@gmail.com (V.A.); ravindra_physicist@ynu.ac.kr (R.K.); dylee@ynu.ac.kr (D.-Y.L.); jshim@ynu.ac.kr (J.S.)

Abstract: Semiconductor-based heterogeneous photocatalytic oxidation processes have received considerable attention for the remediation of toxic pollutants. Herein, InVO₄/NiFe₂O₄ nanocomposites were synthesized using a facile hydrothermal technique. Furthermore, various characterization results revealed the successful loading of NiFe₂O₄ nanoplates over InVO₄ nanosheets, thereby signifying the formation of a heterostructure. The performance of the synthesized photocatalyst was tested for tetracycline (TC) antibiotic removal. The optimized InVO₄/NiFe₂O₄ nanocomposite exhibits maximum photodegradation of TC molecules (96.68%) in 96 min; this is approximately 6.47 and 4.93 times higher than that observed when using NiFe₂O₄ and InVO₄, respectively. The strong interaction between the InVO₄ nanosheets and NiFe₂O₄ nanoplates can improve the visible-light absorption and hinder the recombination of charge carriers, further enhancing the photocatalytic performance. Moreover, hydroxyl radicals play a crucial role in the photodegradation of TC antibiotics.

Keywords: InVO₄; NiFe₂O₄; heterostructure; synergetic effect; tetracycline; visible light



Citation: Sreeram, N.; Aruna, V.; Koutavarapu, R.; Lee, D.-Y.; Shim, J. Novel Indium Vanadium Oxide Nanosheet-Supported Nickel Iron Oxide Nanoplate Heterostructure for Synergistically Enhanced Photocatalytic Degradation of Tetracycline. *Catalysts* **2022**, *12*, 1471. <https://doi.org/10.3390/catal12111471>

Academic Editors: Guan-Ting Pan, Siewhui Chong and Timm Joyce Tieng

Received: 17 October 2022

Accepted: 16 November 2022

Published: 18 November 2022

Publisher's Note: MDPI stays neutral with regard to jurisdictional claims in published maps and institutional affiliations.



Copyright: © 2022 by the authors. Licensee MDPI, Basel, Switzerland. This article is an open access article distributed under the terms and conditions of the Creative Commons Attribution (CC BY) license (<https://creativecommons.org/licenses/by/4.0/>).

1. Introduction

Water is an important resource for every living being on Earth [1,2]. Currently, the demand for clean water is increasing with the exponential growth of the population and the intensification of industrial development [3,4]. In recent years, the rapid growth of science and technology worldwide has promoted the establishment of factories in several sectors, such as semiconductors, microelectronics, and pharmaceuticals. During processing, most factories require substantial amounts of water and discharge wastewater containing harmful contaminants [5,6]. Among these, emerging pharmaceutical contaminants, such as tetracycline (TC) antibiotics, have been identified as one of the most important factors contributing to water pollution [7,8]. Therefore, owing to the extensive use of TC antibiotics and their low biodegradability, trace levels of TC molecules have been detected in various aquatic compartments [9,10]. Additionally, even limited amounts of TC antibiotics in freshwater may result in strains of resistant microorganisms in humans and other organisms [11,12]. Therefore, efficient and low-cost methods must be identified for water remediation [13,14].

Recently, the conservation of natural water resources and improvement of novel methodologies for wastewater treatment have emerged as key environmental issues. Numerous wastewater processing techniques are currently being utilized with variable degrees of efficiency [15,16]. Photocatalysis has been developed as a suitable technique owing to its

economical, non-toxic, safe, and renewable characteristics [17,18]. Moreover, advanced oxidation processes are the most widely used techniques for treating toxic pollutants, such as TC antibiotics, which exhibit high chemical stability and low biodegradability [19,20]. Therefore, semiconductor-based heterogeneous photocatalytic oxidation processes under visible light have received considerable attention for the remediation of toxic pollutants [21,22]. Consequently, novel high-efficiency photocatalysts have attracted significant interest owing to their considerable potential for visible-light utilization [23,24].

Among the various semiconductor metal oxides, indium vanadate has promising properties and is increasingly being used in environmental and energy applications owing to its controllable shape and improved activity [25,26]. InVO_4 has the advantages of low raw cost, nontoxicity, a visible bandgap (~2.2 eV), and excellent photocatalytic performance under visible light [27]. However, the photocatalytic degradation of antibiotics by InVO_4 is limited because of the high recombination rate of photogenerated electrons (e^-) and holes (h^+) [28]. To overcome its inherent shortcomings, the fabrication of InVO_4 -based heterostructured photocatalysts has been extensively analyzed, and this is considered a feasible and efficient strategy. Yao et al. constructed $\text{InVO}_4/\text{TiO}_2$ nanobelts using an electrospinning technique [29]. The as-prepared $\text{InVO}_4/\text{TiO}_2$ nanobelts exhibited excellent photocatalytic activity under solar-light irradiation, owing to their unique morphology and synergetic interactions. Furthermore, $\text{B}_{12}\text{O}_{15}\text{C}_{16}/\text{InVO}_4$ nanocomposites were successfully constructed using an in situ hydrothermal method [30]. The establishment of a Z-scheme among the individual components can significantly improve the separation of charge carriers and enhance the photocatalytic activity. Yuan et al. efficiently synthesized $\text{In}_2\text{S}_3/\text{InVO}_4$ nanocomposites through a facile in situ ion-exchange technique [31]. After 60 min of visible-light irradiation, the prepared nanocomposite degraded TC by 71.4%. The formation of the heterostructure further improved the visible-light absorption ability along with interfacial interactions, thereby indicating photocatalytic activity.

Spinel-structured transition metal oxides, such as nickel ferrite, are abundant and promising minerals with a narrow bandgap (~1.8 eV). Recently, these materials have attracted considerable research interest owing to their unique characteristics [32]. Moreover, the oxidation of these materials has been recognized as a promising technique because of the simple and environmentally friendly reaction process [33]. Accordingly, the construction of an InVO_4 -based heterostructure that is incorporated with NiFe_2O_4 can be regarded as a potential strategy to facilitate charge separation at the interface, thereby enhancing the photocatalytic degradation of TC antibiotics.

Herein, InVO_4 and NiFe_2O_4 are hydrothermally combined to construct a novel two-dimensional $\text{InVO}_4/\text{NiFe}_2\text{O}_4$ heterostructure to remove TC antibiotics from the solution. The structure, morphology, chemical composition, and optical properties of the as-prepared photocatalysts are studied, and their photocatalytic activity is examined by degrading TC. Compared with the pure samples, the $\text{InVO}_4/\text{NiFe}_2\text{O}_4$ heterostructure exhibits higher oxidation ability, faster kinetics, and higher stability owing to the lower radiative recombination rate of charge carriers. Furthermore, a possible charge transfer mechanism with enhanced photocatalytic activity is proposed. The present study provides a new and effective approach for achieving InVO_4 -based heterostructures, which could facilitate the preparation of similar types of materials.

2. Results and Discussion

2.1. X-ray Diffraction (XRD) Analysis

To understand the crystal structure and crystallinity of the $\text{InVO}_4/\text{NiFe}_2\text{O}_4$ nanocomposites, the photocatalysts were characterized using XRD; the results are illustrated in Figure 1. From Figure 1a, the peaks identified at 18.62° , 25.62° , 31.04° , 33.04° , 35.14° , 46.96° , 56.47° , and 60.98° correspond to the (110), (021), (200), (112), (130), (222), (312), and (152) planes of InVO_4 (JCPDS# 00-048-0898). The observed crystal planes match the standard results, thereby confirming the orthorhombic phase of InVO_4 [34]. Furthermore, as shown in Figure 1b, the diffraction peaks at 30.08° , 35.44° , 43.26° , 57.38° , and 62.99°

are in agreement with the (220), (311), (400), (511), and (440) planes of NiFe_2O_4 (JCPDS #00-074-2081) [35]. The XRD patterns of the $\text{InVO}_4/\text{NiFe}_2\text{O}_4$ nanocomposites at different concentrations (Figure 1c–e) reveal the existence of both InVO_4 (@) and NiFe_2O_4 (\$). The loading of NiFe_2O_4 at different concentrations does not cause any deviations in the orthorhombic phase of InVO_4 . However, the intensified InVO_4 diffraction patterns diminish with increasing NiFe_2O_4 concentration, confirming the successful formation of the $\text{InVO}_4/\text{NiFe}_2\text{O}_4$ nanocomposite [36]. No additional peaks are observed in the XRD pattern, indicating that the pattern represents the pure phase, and no impurities are present.

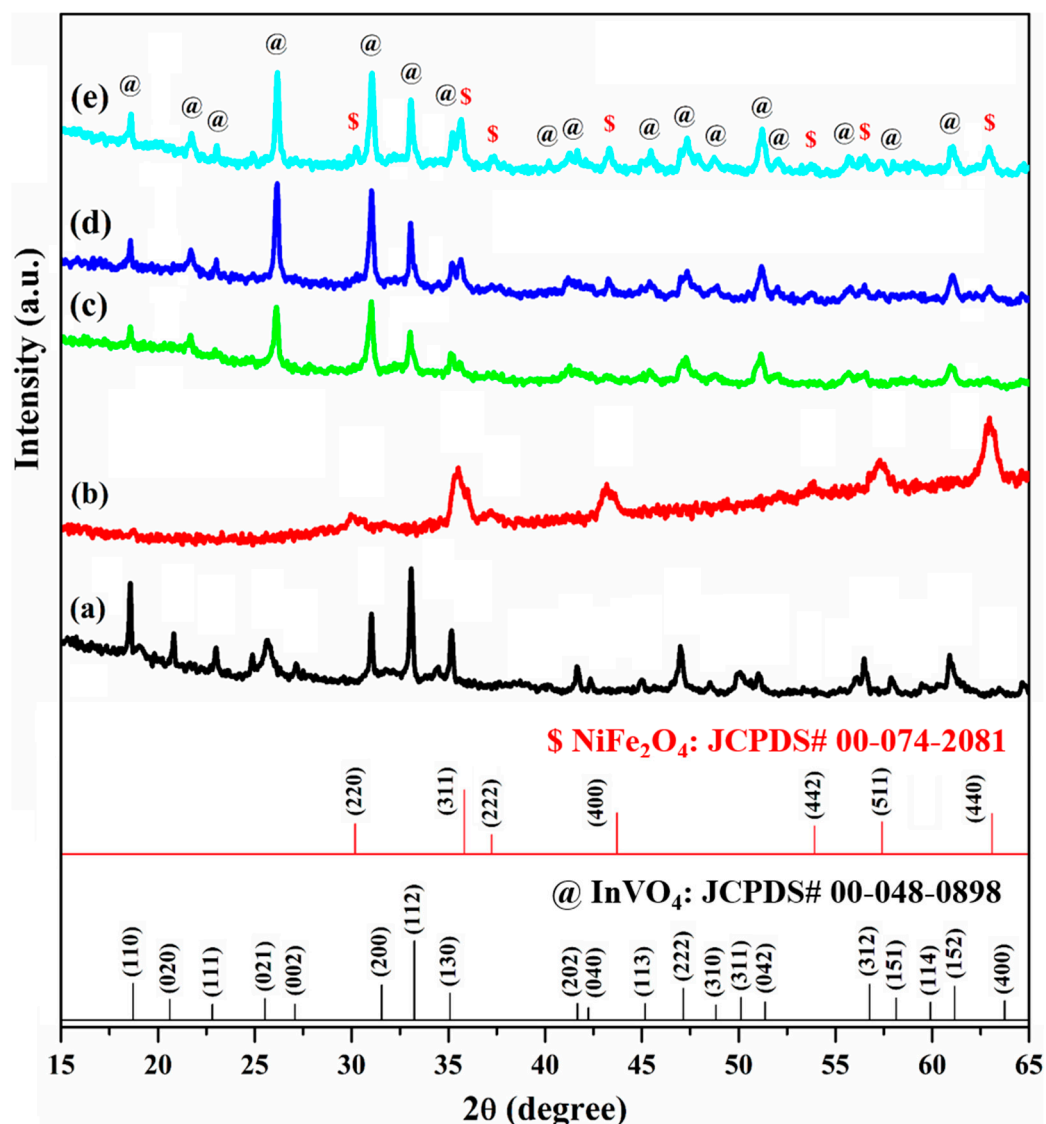


Figure 1. X-ray diffraction patterns of (a) InVO_4 , (b) NiFe_2O_4 , (c) IVNF-2.5, (d) IVNF-5.0, and (e) IVNF-7.5 nanocomposites.

2.2. Morphological Analysis

The morphology of a photocatalyst significantly influences its absorption of light, thereby determining its photocatalytic efficiency. Scanning electron microscopy (SEM), transmission electron microscopy (TEM), and high-resolution TEM (HRTEM) were used to examine the morphologies of InVO_4 , NiFe_2O_4 , and $\text{InVO}_4/\text{NiFe}_2\text{O}_4$ (IVNF-5.0) nanocomposites. As shown in Figure 2a,b, a sheet-like structure was observed for InVO_4 through SEM analysis. SEM images of NiFe_2O_4 (Figure 2c,d) reveal a plate-like morphology with irregular shapes and sizes. Furthermore, Figure 2e,f clearly show that the IVNF-5.0 nanocomposite is composed of InVO_4 nanosheets and NiFe_2O_4 nanoplates. Moreover, the NiFe_2O_4

nanoplates were successfully loaded onto the InVO_4 nanosheets. The energy-dispersive spectroscopy (EDS) analysis of the IVNF-5.0 nanocomposite (Figure 2g) indicated the presence of individual components.

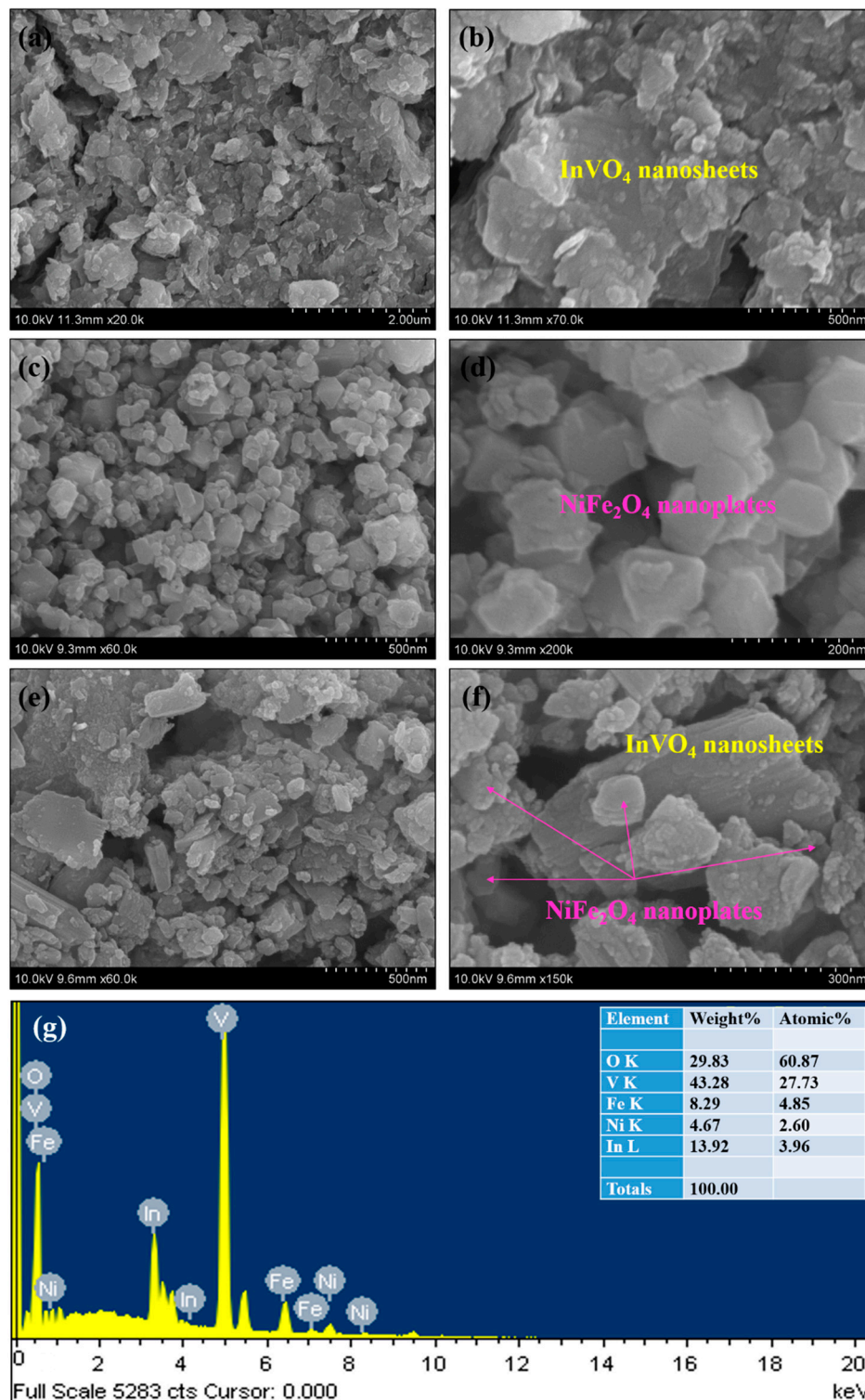


Figure 2. Scanning electron microscopy images of (a,b) InVO_4 nanosheets, (c,d) NiFe_2O_4 nanoplates, (e,f) IVNF-5.0 nanocomposite, and (g) energy-dispersive spectroscopy (EDS) analysis of the IVNF-5.0 nanocomposite.

The TEM images illustrate the formation of InVO_4 nanosheets (Figure 3a), NiFe_2O_4 nanoplates (Figure 3b), and the loading of NiFe_2O_4 nanoplates over InVO_4 nanosheets (Figure 3c). Furthermore, the HRTEM image of IVNF-5.0 confirmed the effective loading of NiFe_2O_4 nanoplates on the InVO_4 nanosheets (Figure 3d). As shown in Figure 3e,f, the lattice spacings of 0.265 and 0.245 nm were attributed to the (112) and (311) crystal planes of InVO_4 and NiFe_2O_4 , respectively [37,38]. Therefore, in terms of the position, the (311) plane of NiFe_2O_4 overlapped with the (112) crystal surface of InVO_4 , confirming the formation of the $\text{InVO}_4/\text{NiFe}_2\text{O}_4$ heterostructure. The EDS color mapping of IVNF-5.0 (Figure 4) further confirmed the existence of In, V, Ni, Fe, and O.

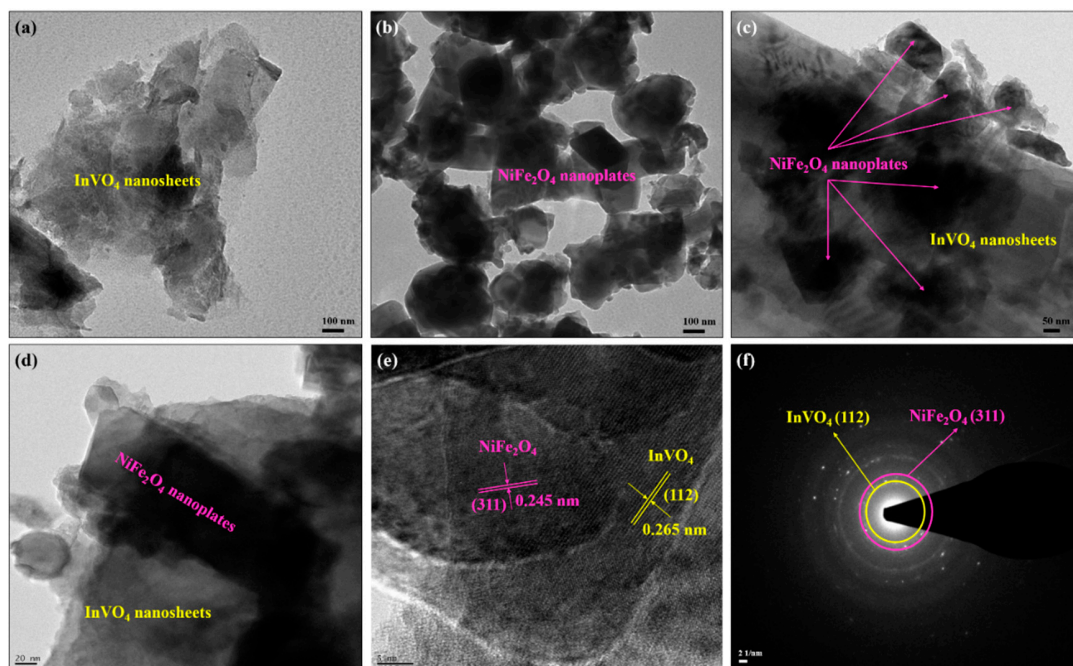


Figure 3. Transmission electron microscopy (TEM) images of (a) InVO_4 , (b) NiFe_2O_4 , and (c) IVNF-5.0; (d) high-resolution TEM image; (e) lattice fringes and (f) selected area electron diffraction patterns of the IVNF-5.0 nanocomposite.

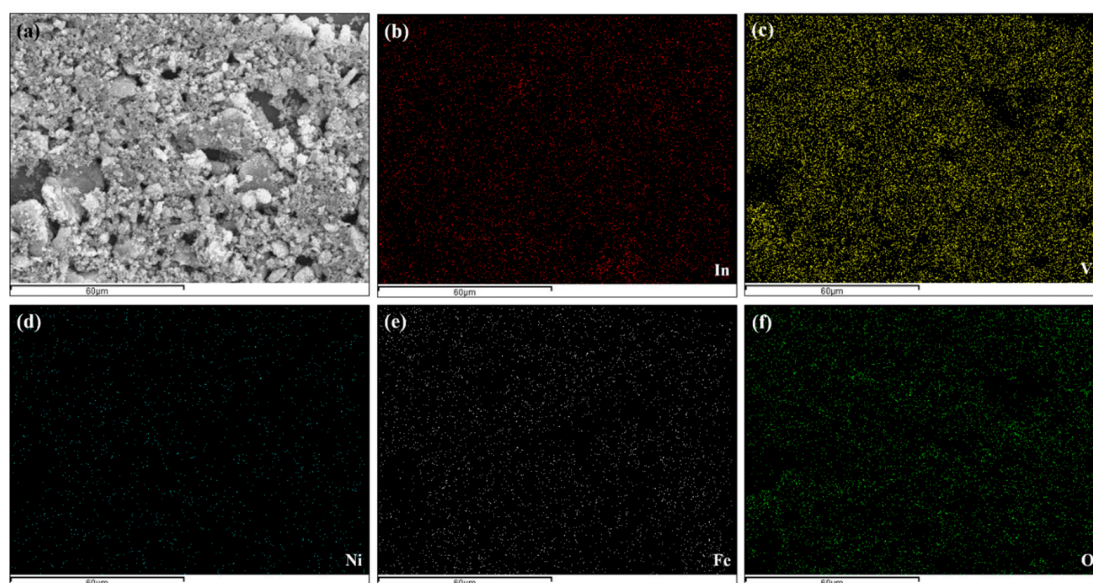


Figure 4. EDS elemental color mapping of the IVNF-5.0 nanocomposite. (a) Mapping region, (b) In, (c) V, (d) Ni, (e) Fe, and (f) O.

2.3. X-ray Photoelectron Spectroscopy (XPS) Analysis

XPS was applied to survey the chemical state of each component of the $\text{InVO}_4/\text{NiFe}_2\text{O}_4$ nanocomposite (Figure 5). In 3d, V 2p, O 1s, Fe 2p, and Ni 2p signals are clearly observed in the XPS general spectrum (Figure 5a) of the IVNF-5.0 photocatalyst. From Figure 5b, the XPS peak fitting of In 3d indicates that the signals at 444.72 and 452.29 eV are consistent with the +3 oxidation state of In $3d_{5/2}$ and In $3d_{3/2}$ energy levels, respectively [39]. As shown in Figure 5c, the XPS spectrum of V 2p exhibits two signals at 516.93 and 524.29 eV, which are assigned to the +5 oxidation state of V $2p_{3/2}$ and V $2p_{1/2}$ energy levels, respectively [40]. The asymmetric O 1s peak (Figure 5d) is divided into two peaks at 529.81 and 531.05 eV, corresponding to the oxygen species in the metal–oxygen bond [41]. The XPS spectrum of Fe 2p (Figure 5e) exhibits two significant signals at 710.85 and 724.16 eV, which are ascribed to Fe $2p_{3/2}$ and Fe $2p_{1/2}$, respectively, and are consistent with metal–oxygen formation [42]. Furthermore, the signals at 716.21 and 732.02 eV are attributed to the satellite signals of Fe^{3+} [43]. As shown in Figure 5f, the XPS spectrum of Ni 2p exhibits two signals at 855.22 and 873.31 eV, corresponding to Ni $2p_{3/2}$ and Ni $2p_{1/2}$, respectively [44]. The signals at 861.51 and 880.32 eV are assigned to the satellite signals of Ni^{2+} [45]. This analysis reveals a strong interaction between InVO_4 and NiFe_2O_4 and confirms the formation of the nanocomposite.

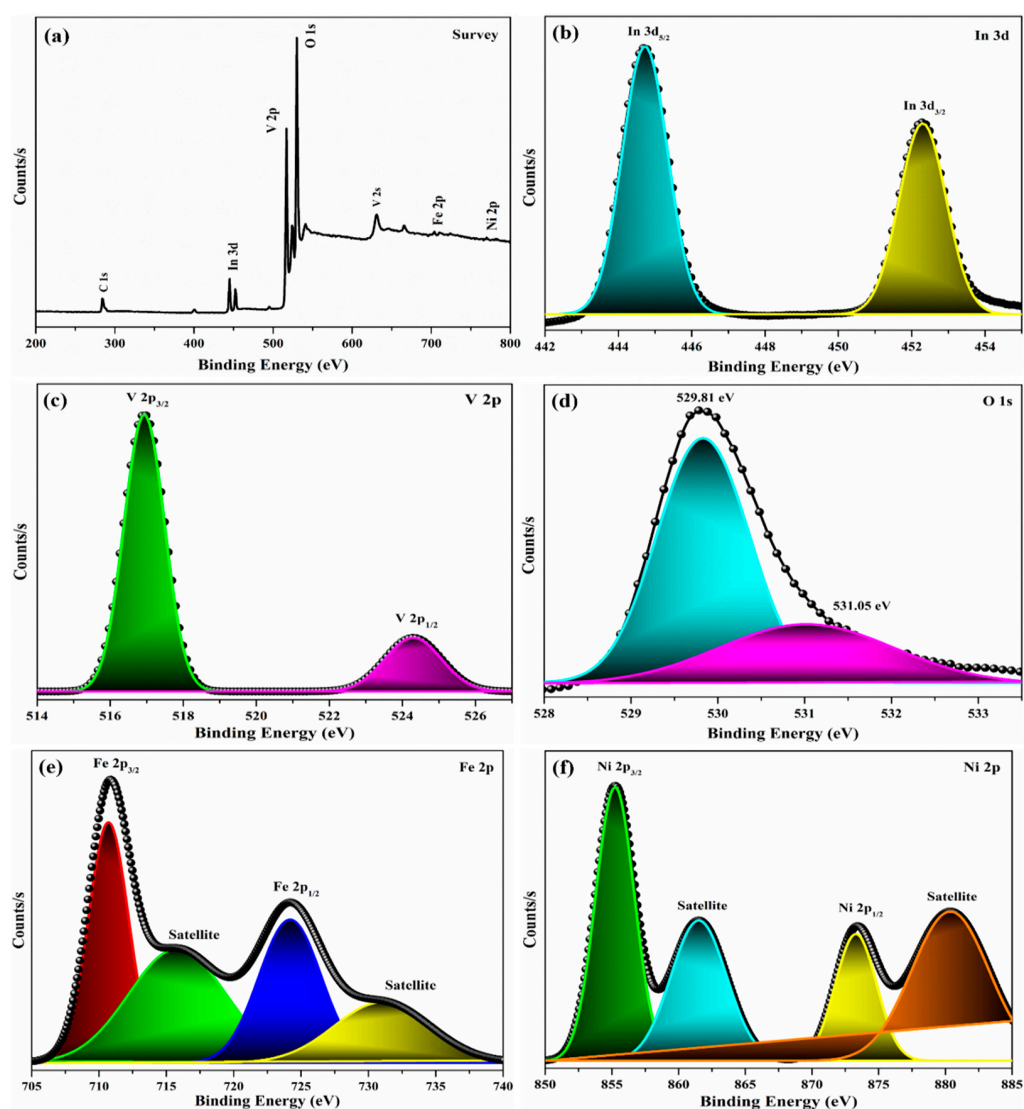


Figure 5. (a) Survey, (b) In 3d, (c) V 2p, (d) O 1s, (e) Fe 2p, and (f) Ni 2p high resolution X-ray photoelectron spectra of the IVNF-5.0 nanocomposite.

2.4. Optical Absorption Analysis

The ability to absorb light in the visible region is a critical property of photocatalysts. Herein, the responses of the prepared samples to light were determined using diffuse reflectance spectroscopy (DRS). The absorption properties for visible light and the bandgaps of InVO_4 , NiFe_2O_4 , and $\text{InVO}_4/\text{NiFe}_2\text{O}_4$ nanocomposites are presented in Figure 6. As shown in Figure 6a, both InVO_4 and NiFe_2O_4 displayed maximum absorbance with band edges at approximately 579 and 680 nm, respectively [46,47]. Moreover, compared with pure InVO_4 , the absorption performance of $\text{InVO}_4/\text{NiFe}_2\text{O}_4$ nanocomposites for visible light was significantly improved toward higher wavelength regions. Therefore, the $\text{InVO}_4/\text{NiFe}_2\text{O}_4$ nanocomposites demonstrate a good response in the visible region, in contrast to the pure samples. This confirms the construction of a heterostructure, which is beneficial for enhanced photocatalytic activity [48]. Furthermore, the bandgaps of InVO_4 , NiFe_2O_4 , and $\text{InVO}_4/\text{NiFe}_2\text{O}_4$ nanocomposites were evaluated based on the corresponding Tauc plots (Figure 6b–d). After extrapolation, the bandgaps of InVO_4 , NiFe_2O_4 , IVNF-2.5, IVNF-5.0, and IVNF-7.5 were measured as 2.142, 1.824, 1.992, 1.938, and 1.852 eV, respectively. A reduction was observed in the bandgap between the pure InVO_4 and the $\text{InVO}_4/\text{NiFe}_2\text{O}_4$ nanocomposites. Consequently, the visible-light absorption capacity of the $\text{InVO}_4/\text{NiFe}_2\text{O}_4$ nanocomposites is better than that of the pure samples.

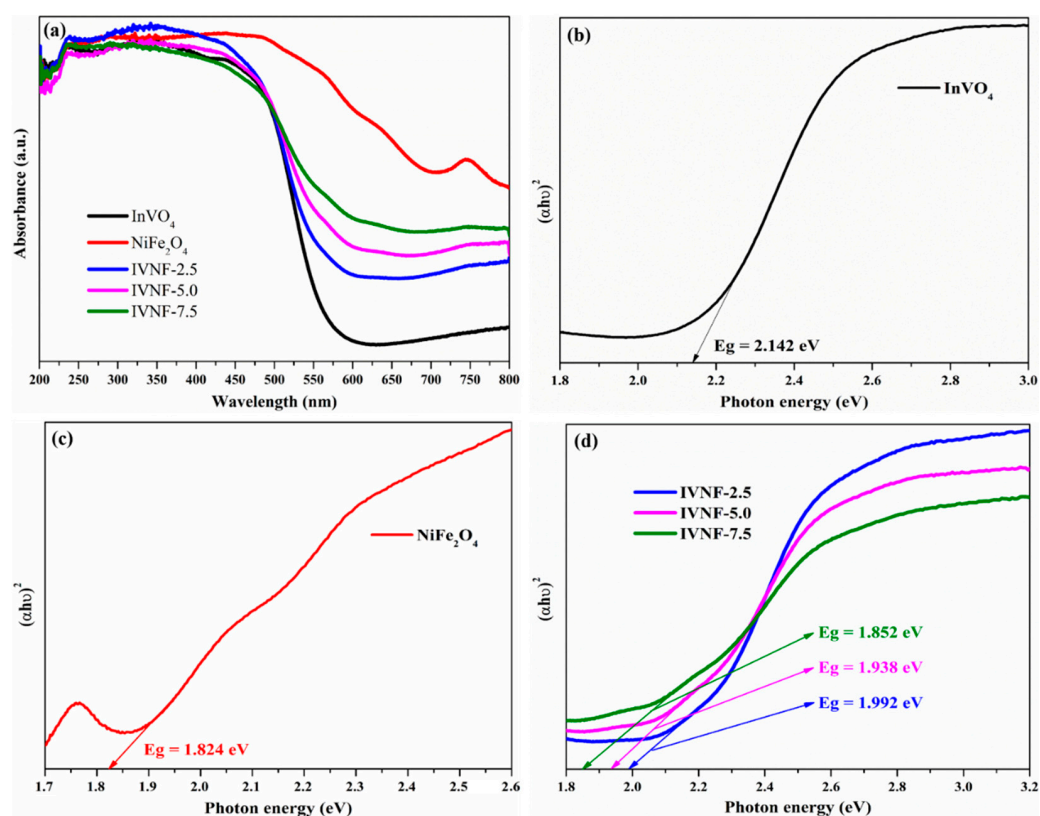


Figure 6. (a) Optical absorption spectra and (b–d) Tauc plots of the synthesized samples.

2.5. Photoluminescence (PL) Analysis

The PL intensity of each sample was tested at the same excitation wavelength (325 nm). The PL spectra of InVO_4 , NiFe_2O_4 , and $\text{InVO}_4/\text{NiFe}_2\text{O}_4$ nanocomposites are shown in Figure 7. For InVO_4 , a strong PL emission peak was observed at approximately 586 nm, which is attributed to the recombination of charge carriers [49]. Furthermore, strong PL emission peaks were observed for NiFe_2O_4 at approximately 465 and 589 nm, which were caused by oxygen vacancies and structural defects [50]. Compared to the pure samples, the PL intensities of the $\text{InVO}_4/\text{NiFe}_2\text{O}_4$ nanocomposites were significantly reduced, and the IVNF-5.0 sample exhibited the lowest PL intensity. Therefore, the $\text{InVO}_4/\text{NiFe}_2\text{O}_4$

nanocomposites display a relatively high ability to separate the photogenerated charge carriers in addition to enhanced photocatalytic performance.

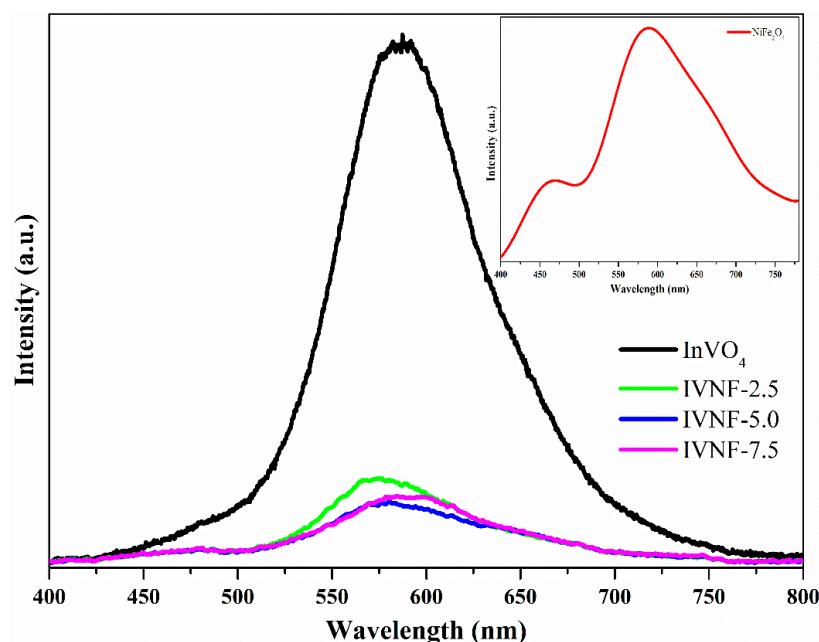


Figure 7. Photoluminescence spectra of the as-prepared samples.

2.6. Photocatalytic Performance

The photodegradation efficiency of the as-synthesized photocatalysts was examined for TC removal under visible light. Before irradiation with visible light, the reactive solution was stirred for 30 min in the dark to ensure that the TC solution was evenly distributed on the photocatalyst surface, and the adsorption process reached equilibrium. The absorbance spectra for the degradation of TC over $\text{InVO}_4/\text{NiFe}_2\text{O}_4$ nanocomposites were recorded every 12 min over a time period of 96 min; the results are presented in Figure 8a,b. The degradation efficiencies of the pure NiFe_2O_4 and InVO_4 samples were 35.26% and 40.97%, respectively. Furthermore, the degradation efficiencies of IVNF-2.5, IVNF-5.0, and IVNF-7.5 were 74.72%, 96.68%, and 81.27%, respectively. Therefore, upon visible-light irradiation, the order of increasing photocatalytic degradation performance is given by: $\text{IVNF-5.0} > \text{IVNF-7.5} > \text{IVNF-2.5} > \text{InVO}_4 > \text{NiFe}_2\text{O}_4$.

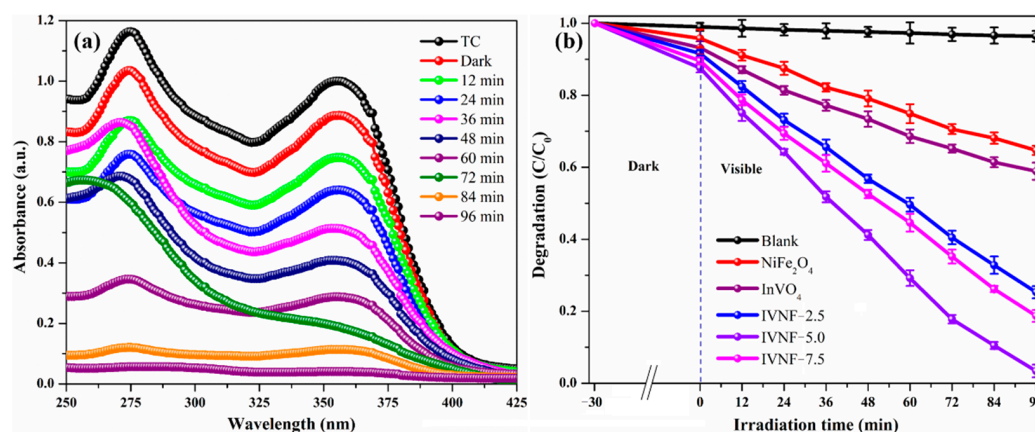


Figure 8. (a) Absorbance spectra for the degradation of tetracycline (TC) over the IVNF-5.0 nanocomposite and (b) degradation efficiency of the as-prepared samples.

To further evaluate the photocatalytic degradation of TC by the $\text{InVO}_4/\text{NiFe}_2\text{O}_4$ nanocomposite, a pseudo-first-order kinetic model was considered. The results of kinetic modeling are presented in Figure 9a,b. The kinetic rate constants of NiFe_2O_4 , InVO_4 , IVNF-2.5, IVNF-5.0, and IVNF-7.5 were calculated to be 0.0045, 0.0059, 0.0132, 0.0291, and 0.0161 min^{-1} , respectively, quantitatively confirming that the IVNF-5.0 photocatalyst is superior to the other samples.

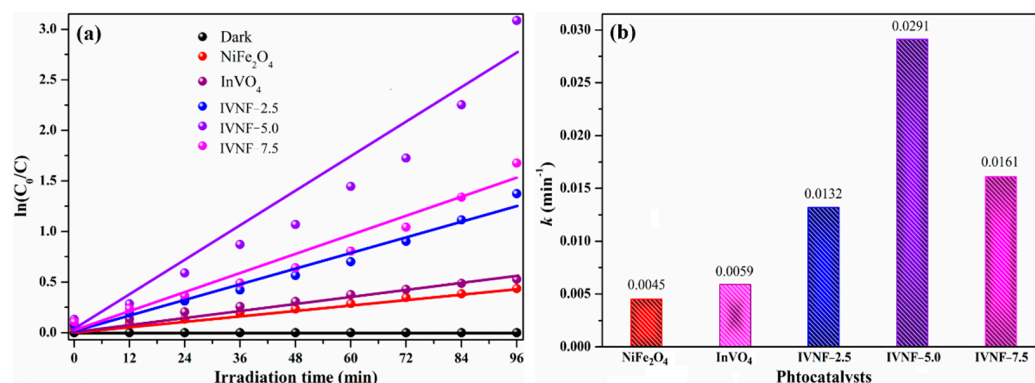


Figure 9. (a) Pseudo-first-order kinetics and (b) kinetic rate constants of the as-prepared catalysts.

Moreover, the rate constant of IVNF-5.0 was 6.47 times that of NiFe_2O_4 and 4.93 times that of InVO_4 . Therefore, the IVNF-5.0 nanocomposite is demonstrated to be a better photocatalyst than the other prepared samples; it significantly enhances the separation ability for photogenerated carriers and retains a strong redox ability, thereby promoting the TC degradation efficiency. The catalytic removal of TC in the present work was compared with that previously reported in the literature, as shown in Table 1. The data reveal the improved photocatalytic activity of the $\text{InVO}_4/\text{NiFe}_2\text{O}_4$ nanocomposites.

Table 1. A comparison of photocatalytic removal of pollutants under visible light using InVO_4 -based nanocomposites with recent examples from the literature.

Photocatalyst	Synthesis Method	Catalyst Loading mg/mL	Removal Dye	Removal Time (min)	Removal Efficiency (%)	Ref.
$\text{InVO}_4/\text{Bi}_{12}\text{O}_{15}\text{C}_{16}$	Hydrothermal	0.50	TC	90	78.85	[30]
$\text{InVO}_4/\text{CeVO}_4$	Electrospinning	0.40	TC	90	92.40	[46]
$\text{InVO}_4/\text{AgVO}_3$	Ion exchange	0.25	RhB	200	99.99	[51]
$\text{InVO}_4/\text{TiO}_2$	Hydrothermal	0.50	RhB	180	55.30	[52]
$\text{InVO}_4/\text{ZnFe}_2\text{O}_4$	Hydrothermal	0.20	MB	240	88.74	[28]
$\text{InVO}_4/\text{N-TiO}_2$	Sol-gel	0.75	NP	90	89.00	[53]
$\text{In}_2\text{S}_3/\text{InVO}_4$	Anion-exchange	0.50	TC	60	71.40	[31]
$\text{InVO}_4/\text{BiVO}_4$	Hydrothermal	0.50	RhB	280	99.78	[54]
rGO/ InVO_4	Electrospinning	0.50	RhB	120	93.00	[55]
$\text{InVO}_4/\text{NiFe}_2\text{O}_4$	Hydrothermal	0.15	TC	96	96.68	Present study

The influence of catalyst loading is an important parameter in determining the degradation of TC by the IVNF-5.0 photocatalyst. The results obtained using various catalyst loadings are shown in Figure 10a. With the gradual increase in catalyst loading, the TC degradation efficiency increases, and the time required for the degradation to attain equilibrium decreases. When the loading of IVNF-5.0 is 10 mg, the TC degradation efficiency is only 78.54%. Furthermore, when the loading of IVNF-5.0 is increased to 15 mg, the TC degradation effect is optimal, with an efficiency of approximately 96.68%. However, when the loading of IVNF-5.0 is further increased to 20 mg, the TC degradation effect is decreased, and its efficiency is approximately 62.33%. As the catalyst loading concentration continues to increase, the rate of degradation begins to decrease at a particular limit because

of the decreased diffusion of light, which hinders the generation of radical species [56]. Furthermore, the stability of the $\text{InVO}_4/\text{NiFe}_2\text{O}_4$ nanocomposite was examined under the optimal experimental conditions for various practical applications. A stability test was conducted with the optimized sample IVNF-5.0 for four cycles under visible light; the results are depicted in Figure 10b. After the IVNF-5.0 photocatalyst degraded TC for 96 min, the photocatalyst was recycled, and the abovementioned process was repeated four times. After four cycles, the TC degradation efficiency reached 93.49%, indicating that the IVNF-5.0 photocatalyst can be effectively reused and has good stability.

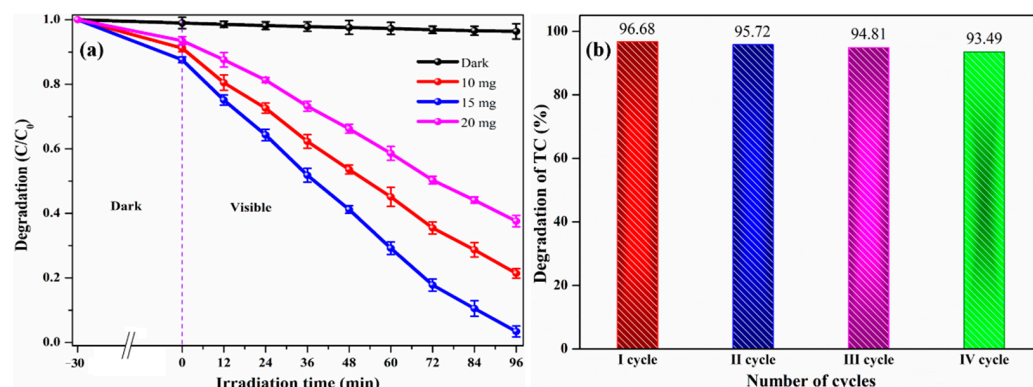


Figure 10. (a) Catalyst loading and (b) stability test over the IVNF-5.0 nanocomposite for the degradation of TC.

Additionally, radical quenching experiments were conducted to identify the influence of free radicals on photodegradation; the results are shown in Figure 11. Herein, BQ, IPA, and TEA were used as scavengers for superoxide ($\bullet\text{O}_2^-$) and hydroxyl ($\bullet\text{OH}$) radicals and h^+ , respectively. As shown in Figure 11, when BQ is added to the reactive solution, TC removal over the IVNF-5.0 photocatalyst decreases considerably to 86.75%. After the addition of TEA, TC removal noticeably decreases to 74.61%. After adding IPA, TC removal is further decreased to 41.29%. Based on these results, $\bullet\text{OH}$ radicals are considered to play a more dominant role than $\bullet\text{O}_2^-$ radicals and h^+ in photocatalytic reactions. Furthermore, to elaborate on the generation and separation efficiency of photoexcited electron–hole pairs, transient photocurrent ($I-t$) tests were conducted. The $I-t$ responses of NiFe_2O_4 , InVO_4 , and $\text{InVO}_4/\text{NiFe}_2\text{O}_4$ nanocomposites under visible light are presented in Figure 11b. The IVNF-5.0 nanocomposite exhibited the strongest response among all samples. Moreover, the $I-t$ response intensity of the IVNF-5.0 nanocomposite was maintained despite several on–off cycles of visible-light irradiation, which demonstrates its excellent photochemical stability.

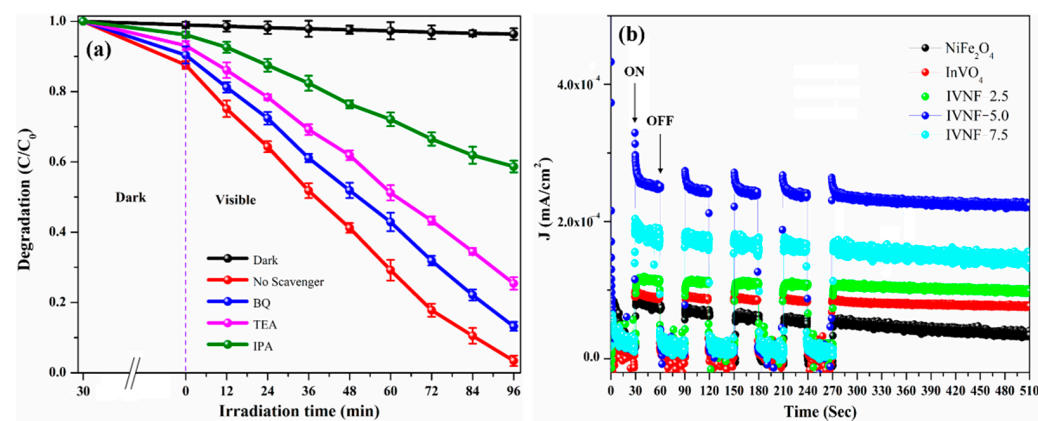


Figure 11. (a) Radical quenching experiment for the degradation of TC over IVNF-5.0 nanocomposite, and (b) $I-t$ curves of the samples under the ON–OFF states.

2.7. Photocatalytic Mechanism

The reaction mechanism of the $\text{InVO}_4/\text{NiFe}_2\text{O}_4$ nanocomposite under visible-light irradiation is shown in Figure 12. Moreover, the valence band (VB) and conduction band (CB) edge potentials of InVO_4 and NiFe_2O_4 were projected using the Butler–Ginley equation to further understand the migration of charge carriers after heterostructure formation [57]. The susceptibility (χ) values of InVO_4 and NiFe_2O_4 are approximately 5.753 and 5.836 eV, respectively. Therefore, InVO_4 has VB and CB potentials of +2.324 and +0.182 eV, respectively, whereas NiFe_2O_4 has VB and CB potentials of +2.248 and +0.424 eV, respectively. During photocatalysis, visible-light irradiation results in the formation of h^+ and e^- , which are transferred to the CB and VB of the $\text{InVO}_4/\text{NiFe}_2\text{O}_4$ heterostructure. Therefore, e^- on the CB of InVO_4 are transferred to the CB of NiFe_2O_4 . Simultaneously, h^+ in the VB of InVO_4 are delivered to the VB of NiFe_2O_4 . Furthermore, e^- in the CB of NiFe_2O_4 can effectively generate $\bullet\text{OH}$ radicals because of their lower negative reduction potential, and they are used for the degradation of TC molecules. The photoinduced h^+ in the VB of NiFe_2O_4 is employed for the exchange of a water molecule and is thereafter converted to $\bullet\text{OH}$ radicals in the visible region. Therefore, $\bullet\text{OH}$ radicals are the strongest oxidants for TC removal. Therefore, a heterojunction can significantly detach electron–hole pairs and produce highly active species on the surface, which enhances the photocatalytic degradation ability.

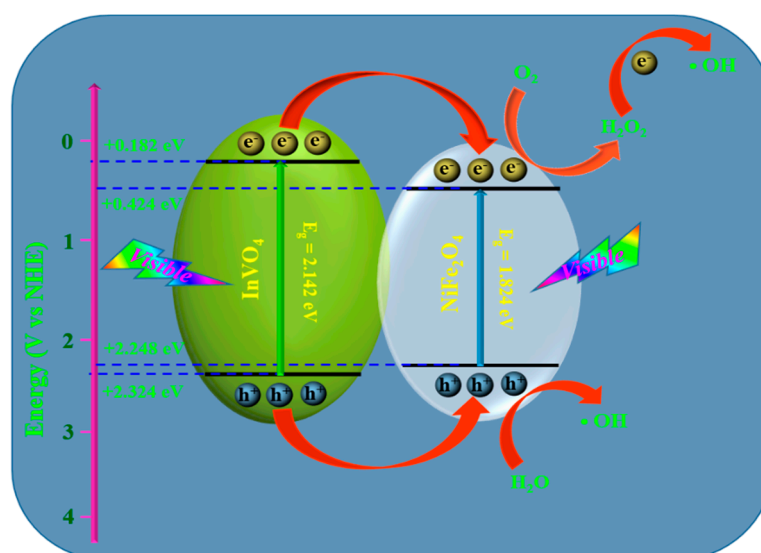


Figure 12. Photocatalytic degradation mechanism of TC molecules by the $\text{InVO}_4/\text{NiFe}_2\text{O}_4$ nanocomposite under visible light.

3. Materials and Methods

3.1. Preparation of InVO_4 Nanosheets

InVO_4 powder was prepared using a hydrothermal method. Initially, NH_4VO_3 and $\text{InCl}_3 \cdot 4\text{H}_2\text{O}$ were added to 60 mL of deionized water at an equal molar ratio (0.1 M) and vigorously stirred for 60 min until dissolution. Subsequently, HNO_3 solution was added dropwise to maintain the pH below 2. The solution was magnetically stirred for 30 min, poured into a Teflon-lined stainless-steel autoclave, heat-treated at 180 °C for 18 h, and naturally cooled to ambient temperature. The resulting products were centrifuged thrice with deionized water and ethanol and dried overnight in an oven at 60 °C.

3.2. Preparation of NiFe_2O_4 Nanoplates

NiFe_2O_4 powder was prepared using a calcination technique. Initially, $\text{FeCl}_3 \cdot 6\text{H}_2\text{O}$ and $\text{NiCl}_2 \cdot 6\text{H}_2\text{O}$ were liquefied in 100 mL of deionized water at a 1:2 molar ratio and stirred for 30 min. The obtained red-brown product was washed thrice and calcinated in a muffle furnace at 500 °C for 3 h.

3.3. Synthesis of InVO₄/NiFe₂O₄ Nanocomposites

Herein, InVO₄/NiFe₂O₄ nanocomposites were obtained using a hydrothermal technique. Typically, 100 mg of the prepared InVO₄ powder and different concentrations of NiFe₂O₄ (2.5, 5.0, and 7.5 mg) powder were separately transferred to 30 mL of deionized water under stirring for 30 min. Different concentrations of NiFe₂O₄ were then added to the InVO₄ solution and stirred vigorously for 1 h. Subsequently, the solution was poured into a Teflon-lined stainless-steel autoclave and heat-treated at 150 °C for 12 h. After being naturally cooled to ambient temperature, the collected products were centrifuged thrice and dried overnight in an oven at 60 °C. For simplicity, the nanocomposites were denoted as IVNF-2.5, IVNF-5.0, and IVNF-7.5. A detailed description of the reagents, characterization, and photodegradation tests can be found in the Supplementary Material.

4. Conclusions

Herein, novel InVO₄/NiFe₂O₄ nanocomposites were successfully prepared using a facile hydrothermal method. XRD analysis confirmed the orthorhombic phase of InVO₄ and spinel structure of NiFe₂O₄. Morphological analysis confirmed the strong interactions between the InVO₄ nanosheets and NiFe₂O₄ nanoplates. From the DRS analysis, a reduction was observed in the bandgap between the pure InVO₄ and InVO₄/NiFe₂O₄ nanocomposites, thereby indicating improved visible-light absorption than that of the pure samples. Furthermore, the optimized IVNF-5.0 nanocomposite was demonstrated to be an efficient photocatalyst for the degradation of TC (96.68%) in 96 min under visible light. The InVO₄/NiFe₂O₄ photocatalyst exhibited good stability and reusability after four cycles. •OH radicals play a more dominant role than •O₂[−] radicals and h⁺ in the photocatalytic reaction. Therefore, the synergetic effect between the InVO₄ nanosheets and NiFe₂O₄ nanoplates significantly enhances the separation ability for the photogenerated carriers and retains their strong redox ability, thereby promoting the TC degradation efficiency.

Supplementary Materials: The following supporting information can be downloaded at: <https://www.mdpi.com/article/10.3390/catal12111471/s1>, Figure S1. XRD pattern of IVNF-5.0 nanocomposite (a) before and (b) after photocatalytic activity; Figure S2. SEM images of IVNF-5.0 nanocomposite (a) before and (b) after photocatalytic activity; Figure S3. TEM images of IVNF-5.0 nanocomposite (a) before and (b) after photocatalytic activity.

Author Contributions: Conceptualization, methodology, formal analysis, and writing—original draft preparation: N.S.; Conceptualization, funding, supervision, and review: V.A.; Conceptualization, methodology, data acquisition, formal analysis, and writing—original draft preparation: R.K.; supervision and review: D.-Y.L.; supervision, funding, and review: J.S. All authors have read and agreed to the published version of the manuscript.

Funding: This study was funded by the Korean Government's National Research Foundation (NRF) (2020R1A2C1012439), Republic of Korea.

Data Availability Statement: Not applicable.

Conflicts of Interest: The authors have no conflicts of interest to declare that are relevant to the content of this article.

References

1. Velempini, T.; Prabakaran, E.; Pillay, K. Recent developments in the use of metal oxides for photocatalytic degradation of pharmaceutical pollutants in water—A review. *Mater. Today Chem.* **2021**, *19*, 100380. [CrossRef]
2. Subhiksha, V.; Kokilavani, S.; Sudheer Khan, S. Recent advances in degradation of organic pollutant in aqueous solutions using bismuth based photocatalysts: A review. *Chemosphere* **2022**, *290*, 133228. [CrossRef] [PubMed]
3. Zia, J.; Fatima, F.; Riaz, U. A comprehensive review on the photocatalytic activity of polythiophene-based nanocomposites against degradation of organic pollutants. *Catal. Sci. Technol.* **2021**, *11*, 6630–6648. [CrossRef]
4. Zuo, W.; Zhang, L.; Zhang, Z.; Tang, S.; Sun, Y.; Huang, H.; Yu, Y. Degradation of organic pollutants by intimately coupling photocatalytic materials with microbes: A review. *Crit. Rev. Biotechnol.* **2021**, *41*, 273–299. [CrossRef] [PubMed]
5. Ateia, M.; Alalm, M.G.; Awfa, D.; Johnson, M.S.; Yoshimura, C. Modeling the degradation and disinfection of water pollutants by photocatalysts and composites: A critical review. *Sci. Total Environ.* **2020**, *698*, 134197. [CrossRef]

6. Gusain, R.; Gupta, K.; Joshi, P.; Khatri, O.P. Adsorptive removal and photocatalytic degradation of organic pollutants using metal oxides and their composites: A comprehensive review. *Adv. Colloid Interface Sci.* **2019**, *272*, 102009. [[CrossRef](#)]
7. Abdurahman, M.H.; Abdullah, A.Z.; Shoparwe, N.F. A comprehensive review on sonocatalytic, photocatalytic, and sonophotocatalytic processes for the degradation of antibiotics in water: Synergistic mechanism and degradation pathway. *Chem. Eng. J.* **2021**, *413*, 127412. [[CrossRef](#)]
8. Chen, G.; Yu, Y.; Liang, L.; Duan, X.; Li, R.; Lu, X.; Yan, B.; Li, N.; Wang, S. Remediation of antibiotic wastewater by coupled photocatalytic and persulfate oxidation system: A critical review. *J. Hazard. Mater.* **2021**, *408*, 124461. [[CrossRef](#)]
9. Abbasnia, A.; Zarei, A.; Yeganeh, M.; Sobhi, H.R.; Gholami, M.; Esrafil, A. Removal of tetracycline antibiotics by adsorption and photocatalytic-degradation processes in aqueous solutions using metal organic frameworks (MOFs): A systematic review. *Inorg. Chem. Commun.* **2022**, *145*, 109959. [[CrossRef](#)]
10. Dai, Y.; Liu, M.; Li, J.; Yang, S.; Sun, Y.; Sun, Q.; Wang, W.; Lu, L.; Zhang, K.; Xu, J.; et al. A review on pollution situation and treatment methods of tetracycline in groundwater. *Sep. Sci. Technol.* **2020**, *55*, 1005–1021. [[CrossRef](#)]
11. Koutavarapu, R.; Jang, W.Y.; Rao, M.C.; Arumugam, M.; Shim, J. Novel BiVO₄-nanosheet-supported MoS₂-nanoflake-heterostructure with synergistic enhanced photocatalytic removal of tetracycline under visible light irradiation. *Chemosphere* **2022**, *305*, 135465. [[CrossRef](#)]
12. Khan, M.E.; Mohammad, A.; Ali, W.; Khan, A.U.; Hazmi, W.; Zakri, W.; Yoon, T. Excellent visible-light photocatalytic activity towards the degradation of tetracycline antibiotic and electrochemical sensing of hydrazine by SnO₂-CdS nanostructures. *J. Clean. Prod.* **2022**, *349*, 131249. [[CrossRef](#)]
13. Ahmed, S.; Rasul, M.G.; Brown, R.; Hashib, M.A. Influence of parameters on the heterogeneous photocatalytic degradation of pesticides and phenolic contaminants in wastewater: A short review. *J. Environ. Manag.* **2011**, *92*, 311–330. [[CrossRef](#)] [[PubMed](#)]
14. Parul; Kaur, K.; Badru, R.; Singh, P.P.; Kaushal, S. Photodegradation of organic pollutants using heterojunctions: A review. *J. Environ. Chem. Eng.* **2020**, *8*, 103666. [[CrossRef](#)]
15. Sharma, K.; Dutta, V.; Sharma, S.; Raizada, P.; Hosseini-Bandegharaei, A.; Thakur, P.; Singh, P. Recent advances in enhanced photocatalytic activity of bismuth oxyhalides for efficient photocatalysis of organic pollutants in water: A review. *J. Ind. Eng. Chem.* **2019**, *78*, 1–20. [[CrossRef](#)]
16. Fauzi, A.A.; Jalil, A.A.; Hassan, N.S.; Aziz, F.F.A.; Azami, M.S.; Hussain, I.; Saravanan, R.; Vo, D.V.N. A critical review on relationship of CeO₂-based photocatalyst towards mechanistic degradation of organic pollutant. *Chemosphere* **2022**, *286*, 131651. [[CrossRef](#)]
17. Sudhaik, A.; Raizada, P.; Rangabhashiyam, S.; Singh, A.; Nguyen, V.-H.; Van Le, Q.; Khan, A.A.P.; Hu, C.; Huang, C.-W.; Ahamad, T.; et al. Copper sulfides based photocatalysts for degradation of environmental pollution hazards: A review on the recent catalyst design concepts and future perspectives. *Surf. Interf.* **2022**, *33*, 102182. [[CrossRef](#)]
18. Qin, K.; Zhao, Q.; Yu, H.; Xia, X.; Li, J.; He, S.; Wei, L.; An, T. A review of bismuth-based photocatalysts for antibiotic degradation: Insight into the photocatalytic degradation performance, pathways and relevant mechanisms. *Environ. Res.* **2021**, *199*, 111360. [[CrossRef](#)]
19. Silvestri, S.; Fajardo, A.R.; Iglesias, B.A. Supported porphyrins for the photocatalytic degradation of organic contaminants in water: A review. *Environ. Chem. Lett.* **2022**, *20*, 731–771. [[CrossRef](#)]
20. He, X.; Kai, T.; Ding, P. Heterojunction photocatalysts for degradation of the tetracycline antibiotic: A review. *Environ. Chem. Lett.* **2021**, *19*, 4563–4601. [[CrossRef](#)]
21. Hu, X.; Ye, Y.; Dong, W.; Huang, Y.; Zhu, M. Quantitative evaluation of structure-activity relationships in heterogeneous photocatalytic oxidation towards organic contaminants. *Appl. Catal. B* **2022**, *309*, 121238. [[CrossRef](#)]
22. Calvete, M.J.F.; Piccirillo, G.; Vinagreiro, C.S.; Pereira, M.M. Hybrid materials for heterogeneous photocatalytic degradation of antibiotics. *Coord. Chem. Rev.* **2019**, *395*, 63–85. [[CrossRef](#)]
23. Zhou, X.; Chen, Y.; Li, C.; Zhang, L.; Zhang, X.; Ning, X.; Zhan, L.; Luo, J. Construction of LaNiO₃ nanoparticles modified g-C₃N₄ nanosheets for enhancing visible light photocatalytic activity towards tetracycline degradation. *Sep. Pur. Technol.* **2019**, *211*, 179–188. [[CrossRef](#)]
24. Khanh Huyen, N.T.; Pham, T.-D.; Dieu Cam, N.T.; Van Quan, P.; Van Noi, N.; Hanh, N.T.; Thanh Tung, M.H.; Dao, V.-D. Fabrication of titanium doped BiVO₄ as a novel visible light driven photocatalyst for degradation of residual tetracycline pollutant. *Ceram. Int.* **2021**, *47*, 34253–34259. [[CrossRef](#)]
25. Yang, R.; Zhang, Y.; Fan, Y.; Wang, R.; Zhu, R.; Tang, Y.; Yin, Z.; Zeng, Z. InVO₄-based photocatalysts for energy and environmental applications. *Chem. Eng. J.* **2022**, *428*, 131145. [[CrossRef](#)]
26. Van Thuan, D.; Nguyen, T.L.; Pham Thi, H.H.; Thanh, N.T.; Ghotekar, S.; Sharma, A.K.; Binh, M.T.; Nga, T.T.; Pham, T.-D.; Cam, D.P. Development of Indium vanadate and Silver deposited on graphitic carbon nitride ternary heterojunction for advanced photocatalytic degradation of residual antibiotics in aqueous environment. *Opt. Mater.* **2022**, *123*, 111885. [[CrossRef](#)]
27. Sreeram, N.; Aruna, V.; Koutavarapu, R.; Lee, D.-Y.; Shim, J. Visible-light-driven indium vanadium oxide nanosheets supported bismuth tungsten oxide nanoflakes heterostructure as an efficient photocatalyst for the tetracycline degradation. *Chemosphere* **2022**, *299*, 134477. [[CrossRef](#)]
28. Wang, Z.; Wang, J.; Pan, Y.; Liu, F.; Lai, Y.; Li, J.; Jiang, L. Preparation and characterization of a novel and recyclable InVO₄/ZnFe₂O₄ composite for methylene blue removal by adsorption and visible-light photocatalytic degradation. *Appl. Surf. Sci.* **2020**, *501*, 144006. [[CrossRef](#)]

29. Yao, L.; Guo, E.; Wei, M.; Wang, Q.; Lu, Q. Electrospun Mesoporous InVO₄/TiO₂ Nanobelts with Enhanced Photocatalytic Properties. *Photochem. Photobiol.* **2019**, *95*, 1122–1130. [[CrossRef](#)]
30. Yao, J.; Huang, L.; Li, Y.; Liu, J.; Liu, J.; Shu, S.; Huang, L.; Zhang, Z. Facile synthesizing Z-scheme Bi₁₂O₁₅C₁₆/InVO₄ heterojunction to effectively degrade pollutants and antibacterial under light-emitting diode light. *J. Colloid Interf. Sci.* **2022**, *627*, 224–237. [[CrossRef](#)]
31. Yuan, X.; Jiang, L.; Liang, J.; Pan, Y.; Zhang, J.; Wang, H.; Leng, L.; Wu, Z.; Guan, R.; Zeng, G. In-situ synthesis of 3D microsphere-like In₂S₃/InVO₄ heterojunction with efficient photocatalytic activity for tetracycline degradation under visible light irradiation. *Chem. Eng. J.* **2019**, *356*, 371–381. [[CrossRef](#)]
32. Gebreslassie, G.; Bharali, P.; Chandra, U.; Sergawie, A.; Baruah, P.K.; Das, M.R.; Alemayehu, E. Hydrothermal Synthesis of g-C₃N₄/NiFe₂O₄ Nanocomposite and Its Enhanced Photocatalytic Activity. *Appl. Organomet. Chem.* **2019**, *33*, e5002. [[CrossRef](#)]
33. Mishra, P.; Behera, A.; Kandi, D.; Parida, K. Facile construction of a novel NiFe₂O₄@P-doped g-C₃N₄ nanocomposite with enhanced visible-light-driven photocatalytic activity. *Nanoscale Adv.* **2019**, *1*, 1864–1879. [[CrossRef](#)] [[PubMed](#)]
34. Wang, C.; Yang, B.; Liu, H.; Xia, F.; Xiao, J. Potentiometric ammonia sensor with InVO₄ sensing electrode. *Sens. Actuators B* **2020**, *316*, 128140. [[CrossRef](#)]
35. Atla, R.; Shaik, B.; Oh, T.H. NiFe₂O₄ nanoplates decorated on MoS₂ nanosheets as an effective visible light-driven heterostructure photocatalyst for the degradation of methyl orange. *J. Mater. Sci. Mater. Electron.* **2022**, 1–14. [[CrossRef](#)]
36. Shi, Z.; Lan, L.; Li, Y.; Yang, Y.; Zhang, Q.; Wu, J.; Zhang, G.; Zhao, X. Co₃O₄/TiO₂ Nanocomposite Formation Leads to Improvement in Ultraviolet-Visible-Infrared-Driven Thermocatalytic Activity Due to Photoactivation and Photocatalysis–Thermocatalysis Synergetic Effect. *ACS Sustain. Chem. Eng.* **2018**, *6*, 16503–16514. [[CrossRef](#)]
37. Hafeez, H.Y.; Lakhera, S.K.; Shankar, M.V.; Neppolian, B. Synergetic improvement in charge carrier transport and light harvesting over ternary InVO₄-g-C₃N₄/rGO hybrid nanocomposite for hydrogen evolution reaction. *Int. J. Hydrogen Energy* **2020**, *45*, 7530–7540. [[CrossRef](#)]
38. Zhao, X.; Zhang, Y.-L.; Wang, X.-X.; Shi, H.-L.; Wang, W.-Z.; Cao, M.-S. Enhanced microwave absorption properties of NiFe₂O₄ nanocrystal deposited reduced graphene oxides. *J. Mater. Sci. Mater. Electron.* **2016**, *27*, 11518–11523. [[CrossRef](#)]
39. Dang, M.T.; Lefebvre, J.; Wuest, J.D. Recycling Indium Tin Oxide (ITO) Electrodes Used in Thin-Film Devices with Adjacent Hole-Transport Layers of Metal Oxides. *ACS Sustain. Chem. Eng.* **2015**, *3*, 3373–3381. [[CrossRef](#)]
40. Yang, H.; Wang, P.; Zhang, J.; Zhang, L.; Yan, J. Microwave hydrothermal synthesis of SbVO₄ nanospheres as anode materials for sodium ion batteries. *Ionics* **2020**, *26*, 1267–1273. [[CrossRef](#)]
41. McInnes, A.; Plant, S.R.; Ornelas, I.M.; Palmer, R.E.; Wijayantha, K.G.U. Enhanced photoelectrochemical water splitting using oxidized mass-selected Ti nanoclusters on metal oxide photoelectrodes. *Sustain. Energy Fuels* **2017**, *1*, 336–344. [[CrossRef](#)]
42. Rajan, A.; Sharma, M.; Sahu, N.K. Assessing magnetic and inductive thermal properties of various surfactants functionalised Fe₃O₄ nanoparticles for hyperthermia. *Sci. Rep.* **2020**, *10*, 15045. [[CrossRef](#)] [[PubMed](#)]
43. Li, L.; Ma, P.; Hussain, S.; Jia, L.; Lin, D.; Yin, X.; Lin, Y.; Cheng, Z.; Wang, L. FeS₂/carbon hybrids on carbon cloth: A highly efficient and stable counter electrode for dye-sensitized solar cells. *Sustain. Energy Fuels* **2019**, *3*, 1749–1756. [[CrossRef](#)]
44. Cheng, M.; Fan, H.; Song, Y.; Cui, Y.; Wang, R. Interconnected hierarchical NiCo₂O₄ microspheres as high-performance electrode materials for supercapacitors. *Dalton Trans.* **2017**, *46*, 9201–9209. [[CrossRef](#)] [[PubMed](#)]
45. Gao, Y.; Mi, L.; Wei, W.; Cui, S.; Zheng, Z.; Hou, H.; Chen, W. Double Metal Ions Synergistic Effect in Hierarchical Multiple Sulfide Microflowers for Enhanced Supercapacitor Performance. *ACS Appl. Mater. Interf.* **2015**, *7*, 4311–4319. [[CrossRef](#)] [[PubMed](#)]
46. Ding, W.; Lin, X.; Ma, G.; Lu, Q. Designed formation of InVO₄/CeVO₄ hollow nanobelts with Z-scheme charge transfer: Synergistically boosting visible-light-driven photocatalytic degradation of tetracycline. *J. Environ. Chem. Eng.* **2020**, *8*, 104588. [[CrossRef](#)]
47. Sankaranarayanan, R.; Shailajha, S.; Mubina, M.S.K.; Anilkumar, C.P. Effect of Ni²⁺ and Fe³⁺ Ion Concentrations on Structural, Optical, Magnetic, and Impedance Response of NiFe₂O₄ Nanoparticles Prepared by Sol-Gel Process. *J. Supercond. Novel Magn.* **2020**, *33*, 3631–3642. [[CrossRef](#)]
48. Kite, S.V.; Kadam, A.N.; Sathe, D.J.; Patil, S.; Mali, S.S.; Hong, C.K.; Lee, S.W.; Garadkar, K.M. Nanostructured TiO₂ Sensitized with MoS₂ Nanoflowers for Enhanced Photodegradation Efficiency toward Methyl Orange. *ACS Omega* **2021**, *6*, 17071–17085. [[CrossRef](#)]
49. Faisal, M.; Iqbal, A.; Adam, F.; Jothiramalingam, R. Effect of Cu doping on the photocatalytic activity of InVO₄ for hazardous dye photodegradation under LED light and its mechanism. *Water Sci. Technol.* **2021**, *84*, 576–595. [[CrossRef](#)]
50. Babu, B.; Koutavarapu, R.; Shim, J.; Yoo, K. SnO₂ quantum dots decorated NiFe₂O₄ nanoplates: 0D/2D heterojunction for enhanced visible-light-driven photocatalysis. *Mater. Sci. Semicond. Process.* **2020**, *107*, 104834. [[CrossRef](#)]
51. Zhang, X.; Zhang, J.; Yu, J.; Zhang, Y.; Cui, Z.; Sun, Y.; Hou, B. Fabrication of InVO₄/AgVO₃ heterojunctions with enhanced photocatalytic antifouling efficiency under visible-light. *Appl. Catal. B* **2018**, *220*, 57–66. [[CrossRef](#)]
52. Shen, J.; Yang, H.; Feng, Y.; Cai, Q.; Shen, Q. Synthesis of 3D hierarchical porous TiO₂/InVO₄ nanocomposites with enhanced visible-light photocatalytic properties. *Solid State Sci.* **2014**, *32*, 8–12. [[CrossRef](#)]
53. Sandra, C.D.; Alberto, E.G.; Ricardo, G. Heterojunction formation on InVO₄/N-TiO₂ with enhanced visible light photocatalytic activity for reduction of 4-NP. *Mater. Sci. Semicond. Process.* **2019**, *89*, 201–211. [[CrossRef](#)]
54. Zhang, X.; Zhang, J.; Yu, J.; Zhang, Y.; Yu, F.; Jia, L.; Tan, Y.; Zhu, Y.; Hou, B. Enhancement in the photocatalytic antifouling efficiency over cherimoya-like InVO₄/BiVO₄ with a new vanadium source. *J. Colloid Interface Sci.* **2019**, *533*, 358–368. [[CrossRef](#)]

55. Ma, D.; Zhang, Y.; Gao, M.; Xin, Y.; Wu, J.; Bao, N. RGO/InVO₄ hollowed-out nanofibers: Electrospinning synthesis and its application in photocatalysis. *Appl. Surf. Sci.* **2015**, *353*, 118–126. [[CrossRef](#)]
56. Rahman, K.H.; Kar, A.K. Influence of catalyst loading on photocatalytic degradation efficiency of CTAB-assisted TiO₂ photocatalyst towards methylene blue dye solution. *Bull. Mater. Sci.* **2022**, *45*, 18. [[CrossRef](#)]
57. Grubač, Z.; Katić, J.; Metikoš-Huković, M. Energy-Band Structure as Basis for Semiconductor n-Bi₂S₃/n-Bi₂O₃ Photocatalyst Design. *J. Electrochem. Soc.* **2019**, *166*, H433–H437. [[CrossRef](#)]